JGR Solid Earth

RESEARCH ARTICLE
10.1029/2024JB030039

Seamount Magnetism From Helbig's Integrals: Application to the Rano Rahi Seamount Field (East Pacific Rise 17°–19°S)

F. Caratori Tontini[1]

[1]DISTAV, University of Genoa, Genoa, Italy

Key Points:

- I propose a reliable algorithm to determine seamount magnetization direction
- Crustal magnetization polarities of Rano Rahi Seamounts are consistent with the geomagnetic polarity time scale intervals
- The average constructional volume rate for each volcano in the Rano Rahi is in the range 0.5×10^{-3}–1.3×10^{-3} km^3/yr

Correspondence to:
F. Caratori Tontini,
fabio.caratori.tontini@unige.it

Citation:
Caratori Tontini, F. (2025). Seamount magnetism from Helbig's integrals: Application to the Rano Rahi Seamount Field (East Pacific Rise 17°–19°S). *Journal of Geophysical Research: Solid Earth*, *130*, e2024JB030039. https://doi.org/10.1029/2024JB030039

Received 13 AUG 2024
Accepted 26 JAN 2025

Author Contribution:
Conceptualization: F. Caratori Tontini
Methodology: F. Caratori Tontini
Software: F. Caratori Tontini
Writing – review & editing: F. Caratori Tontini

Abstract Determining accurate magnetization directions is essential for interpreting magnetic anomalies and inferring the subseafloor crustal magnetization of submarine volcanoes. Furthermore, magnetization directions can be used to determine the polarity of the Earth's magnetic field at the time the seamount was formed, which in turn can be correlated with the geomagnetic polarity time scale to provide independent means of dating submarine volcanic edifices. Here I show a new method to determine seamount magnetization directions from observed magnetic anomalies, based on their fundamental properties expressed by Helbig's infinite integrals, and I propose practical strategies to reduce effects associated with limited-size surveys. The method provides more reliable results than conventional methods based on semi-norm minimization, as demonstrated by the example of Ita Mai Tai Seamount on the Magellan Seamount Trail. The systematic application of this method to the Rano Rahi Seamount Field, in proximity of the East Pacific Rise (EPR) 17°–19°S shows a pattern of alternating crustal magnetization polarities, consistent with few available radiometric ages and with the geomagnetic polarity time scale for the last 3.5 Ma. The corresponding correlation provides an independent tool for dating seamounts in this region, yielding an average constructional volume rate in the range ~0.5×10^{-3}–1.3×10^{-3} km^3/yr for each volcano, which implies a significant contribution of the total magma supply rate is produced off-axis.

Plain Language Summary Submarine volcanoes produce measurable magnetic anomalies. Detailed analysis of these magnetic anomalies provides an important tool to investigate the internal structure of these volcanoes. More importantly, the directions of the magnetic field generated by submarine volcanoes record the polarity of the magnetic field of the Earth at the time the volcano was formed, providing an independent means of dating. In this paper I propose a new method to determine seamount magnetization directions from observed magnetic anomalies, and I apply this method to the Rano Rahi Seamount Field, in proximity of the mid-ocean ridge known as East Pacific Rise (EPR), between 17°S and 19°S. I find that by correlating these result with the pattern of alternating polarities of the Earth's magnetic field in the last 3.5 million years, I obtain an average constructional volume rate in the range ~0.0005–0.0013 cubic kilometers per year for these submarine volcanoes, which implies a significant contribution of magma is produced further away from the main axis of the oceanic ridge.

1. Introduction

Interpretation of magnetic anomalies is complicated by the variable direction of the magnetization of the source, which is a consequence of the dipolar nature of the magnetic field. The assumption that the magnetization is parallel to the local geomagnetic field is quite often not appropriate (e.g., Clark, 2014), as the Natural Remanent Magnetization (NRM) records the direction of the geomagnetic field at the location and at the time when the rocks formed and cooled below the Curie temperature. The positions and orientations of rocks change over geologic time, dominated by further tectonic translation and/or rotations, or structural movements, and thus the local geomagnetic field can have a completely different direction relative to the primary NRM recorded when the rock was formed. Before any attempt is made to interpret magnetic anomalies it is thus essential to estimate the magnetization direction, as wrong assumptions can result in misleading interpretation (e.g., Clark, 2014).

The magnetization direction is then an essential information for the determination of the internal structure of seamounts from the interpretation of their magnetic anomalies. Measurements of magnetic properties from rock samples or boreholes can help to constrain the magnetization direction, but extensive sampling of the source is

practically impossible, particularly when dealing with submarine volcanoes. More commonly, the direction of magnetization is directly determined by the magnetic anomaly itself (e.g., Clark, 2014), particularly for anomalies that can be related to topographic/bathymetric features, such as seamounts. In this case, additional simplifying assumptions are commonly introduced, as for example, the hypothesis of uniform magnetization, where the magnetization direction can be different relative to the local geomagnetic field, but is homogeneous throughout the source volume (e.g., Parker, 1988).

Seamount magnetism can indeed be strongly affected by non-uniform components caused for example, by lithological variability and/or construction duration spanning multiple magnetic polarity intervals (e.g., Gee et al., 1998; McNutt, 1986). Contribution of induced and viscous magnetization components can also complicate the magnetization pattern (e.g., Gee et al., 1989; Gee et al., 1993). Nevertheless, when these effects are small, magnetic anomalies can still provide an independent method of dating submarine volcanism and to determine the time span of seamount construction when radiometric ages are not available (e.g., Maia et al., 2005; Romano et al., 2022).

Furthermore, paleomagnetic poles can be derived from the uniform magnetization component of seamounts, providing important information on tectonic plate motions (e.g., Harrison et al., 1975; Lee et al., 2003; Sager & Koppers, 2000) and hot-spot dynamics (e.g., Sager et al., 2005). Despite some limitations in the interpretation of seamount paleomagnetic results (e.g., Cottrell & Tarduno, 2000), the large amount of seamount magnetic anomaly data, and the demonstrated consistency of paleomagnetic data from similar age seamounts indicate that these data can still contribute to the definition of Apparent Polar Wander Path (APWP) and plate kinematics. Paleomagnetic investigations from seamount magnetic anomalies become particularly effective when combined to other more accurate paleomagnetic data -sets, such as magnetic inclination data from drilling, or other geophysical methods, such as analysis of skewness of magnetic anomalies (e.g., Acton & Gordon, 1991; Zheng et al., 2018).

Here I apply the integral method originally developed by Helbig (1963) to estimate the magnetization directions, to seamount magnetism. I will show how the accuracy of the original method can be improved by introducing bathymetric constraints within a statistical approach aimed at determining an average magnetization direction and a corresponding confidence ellipse. I discuss the reliability of the method by showing the results of some synthetic tests, as well as by calculating the magnetization direction and paleopole for Ita Mai Tai, which was previously investigated by other authors (Lee et al., 2003). Finally, I will discuss the results from the analysis of magnetic anomalies associated with the Rano Rahi Seamount Field, in proximity of the East Pacific Rise (EPR), 17°–19°S. I will place constraints on the relative ages of these seamounts with respect to the EPR seafloor spreading, as well as determining the average constructional rates.

2. Methods and Practical Strategies

2.1. Helbig's Integral Theory Applied to Seamount Magnetization

Similarly to the approach of Parker (1988), I model the magnetization of a seamount assuming a uniform direction and I decompose the total magnetization $\boldsymbol{J}^t$ using a constant vector component $\boldsymbol{J}^u$, and a residual component $\boldsymbol{J}^r$ (which is a function of position inside the seamount and has zero-mean) along the same direction of the vector $\boldsymbol{J}^u$, as follows:

$$\boldsymbol{J}^t = \boldsymbol{J}^u + \boldsymbol{J}^r, \tag{1}$$

with the aim of using the integral theory to estimate $\boldsymbol{J}^u$, and then subtract the corresponding effect from the observed data to invert the residual anomaly for the modulus of the residual component $J^r = |\boldsymbol{J}^r|$, as this describes the heterogeneities in the seamount structure. I summarize here the main equations; a detailed description of the integral theory is in the original paper by Helbig (1963) and the subsequent applications of Phillips (2004) and Caratori Tontini and Pedersen (2008), for example. Assuming that the magnetic observations have been collected at elevation $z = 0$ (i.e., sea-level), the following system of equations (also known as Helbig's Integrals *HI*) for the vector components of the magnetic moment $\boldsymbol{M}$ of the seamount holds:

$$HI:\begin{cases} M_x = \iiint_{V_s} J_x^u \mathrm{dV_s} = -\frac{2}{\mu_0}\int_{-\infty}^{+\infty}\int_{-\infty}^{+\infty} x\cdot\Delta T_z\ \mathrm{dxdy} \\ M_y = \iiint_{V_s} J_y^u \mathrm{dV_s} = -\frac{2}{\mu_0}\int_{-\infty}^{+\infty}\int_{-\infty}^{+\infty} y\cdot\Delta T_z\ \mathrm{dxdy} \\ M_z = \iiint_{V_s} J_z^u \mathrm{dV_s} = -\frac{1}{\mu_0}\int_{-\infty}^{+\infty}\int_{-\infty}^{+\infty} (x\cdot\Delta T_x + y\cdot\Delta T_y)\ \mathrm{dxdy} \end{cases}, \quad (2)$$

where

1. $\mu_0 = 4\pi \times 10^{-7}$ H/m is the vacuum magnetic permeability;
2. x, y are coordinates over the magnetic observation surface (horizontal plane at $z = 0$);
3. V_s is the seamount volume;
4. $(\Delta T_x, \Delta T_y, \Delta T_z)$ are the vector components of the scalar magnetic anomaly ΔT.

The infinite integrals of the magnetic field components can be thus used to calculate the magnetic moments of the seamount, and in turn the uniform magnetization inclination I, declination D and intensity $J^u = |\boldsymbol{J}^u|$ as follows:

$$\begin{cases} I = \tan^{-1}\left(\dfrac{M_z}{\sqrt{M_x^2 + M_y^2}}\right) \\ D = \tan^{-1}\left(\dfrac{M_y}{M_x}\right) \\ J^u = \dfrac{\sqrt{M_x^2 + M_y^2 + M_z^2}}{V_s} \end{cases}. \quad (3)$$

In practice truncated integrals are calculated from the observed magnetic anomalies over the finite domain corresponding to the survey area, which means that only a fraction of the magnetic moments can be determined.

An iterative approach is used to estimate the infinite integrals (Figure 1). Initial step requires to calculate the starting truncated Helbig's integral HI_o from the observed magnetic anomaly ΔT_o, regularly sampled on the finite domain of the survey area. Using Equation 2 the initial values for the magnetic moments (M_x^0, M_y^0, M_z^0) are also determined. Iterations proceed as follows:

1. At iteration i use the magnetic moments $(M_x^{i-1}, M_y^{i-1}, M_z^{i-1})$ determined at iteration i-1 to estimate corresponding Helbig's integrals HI^i over an infinite domain using Equation 2 (from right to left);
2. Calculate the magnetic anomaly ΔT_u^{i-1} from the uniform magnetization distribution with parameters $(I^{i-1}, D^{i-1}, J^{ui-1})$ determined at iteration $i-1$ and calculate corresponding truncated Helbig's integrals HI_u^i over the finite domain;
3. Subtract the truncated integrals HI_u^i from the infinite integrals HI^i;
4. Restore the effect of the observed data by adding the truncated integrals HI_o calculated from the magnetic observations over the finite domain, that is, calculate $HI_o + HI^i - HI_u^i$;
5. Use Equation 2 (from left to right) to calculate revised magnetic moment vector $\boldsymbol{M}^i$ from the new set of integrals $HI_o + HI^i - HI_u^i$ and use Equation 3 to calculate uniform revised magnetization parameters (I^i, D^i, J^{ui});
6. Calculate the residual magnetic anomaly $\Delta T_r^i = \Delta T_o - \Delta T_u^i$ by subtracting the magnetic anomaly from uniform magnetization ΔT_u^i from the observed magnetic anomalies ΔT_o. Finally invert ΔT_r^i using a least-squares approach to determine the residual magnetization distribution J^{ri} using the magnetization directions (I^i, D^i).

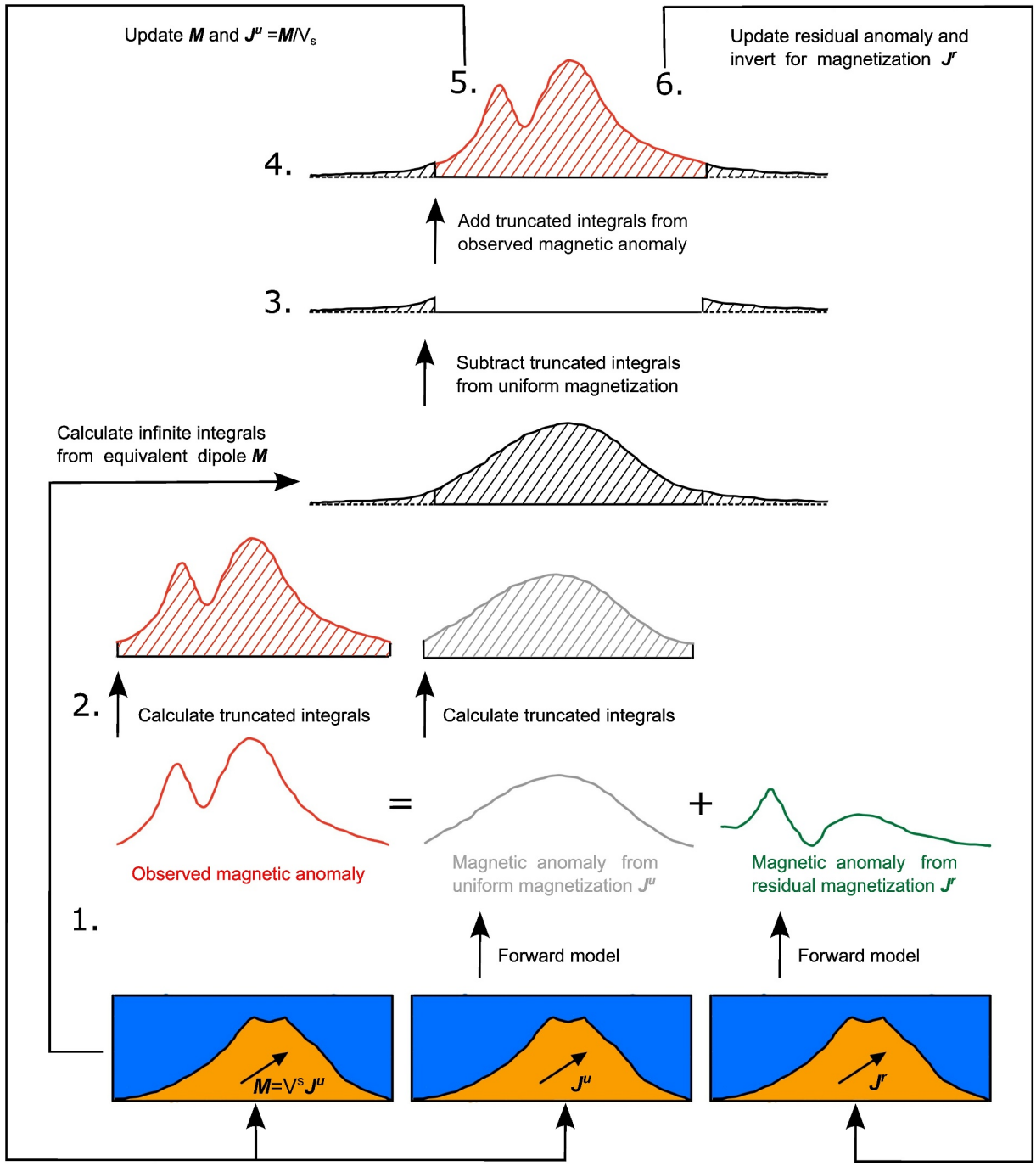

Figure 1. Description of the algorithm and iteration process. Numbers 1.-6. are the steps described in Section 2.1. The red, gray and green profiles are the observed magnetic anomaly, the magnetic anomaly from the uniform model, and the magnetic anomaly from the residual magnetization model, respectively. Helbig's integrals are represented by the set of inclined parallel lines under the corresponding magnetic profiles.

Steps 1.–6. Are repeated until the change in the magnetization parameters is smaller than a specified tolerance value. Convergence where variation of the angular parameters is less than 1% is typically reached with a number of iterations <15.

Figure 2 shows the results of the iterations on a selected synthetic test. The bathymetry model is shown in Figure 2a. In this specific case I assumed a regional geomagnetic field with inclination 60° and declination 0°,

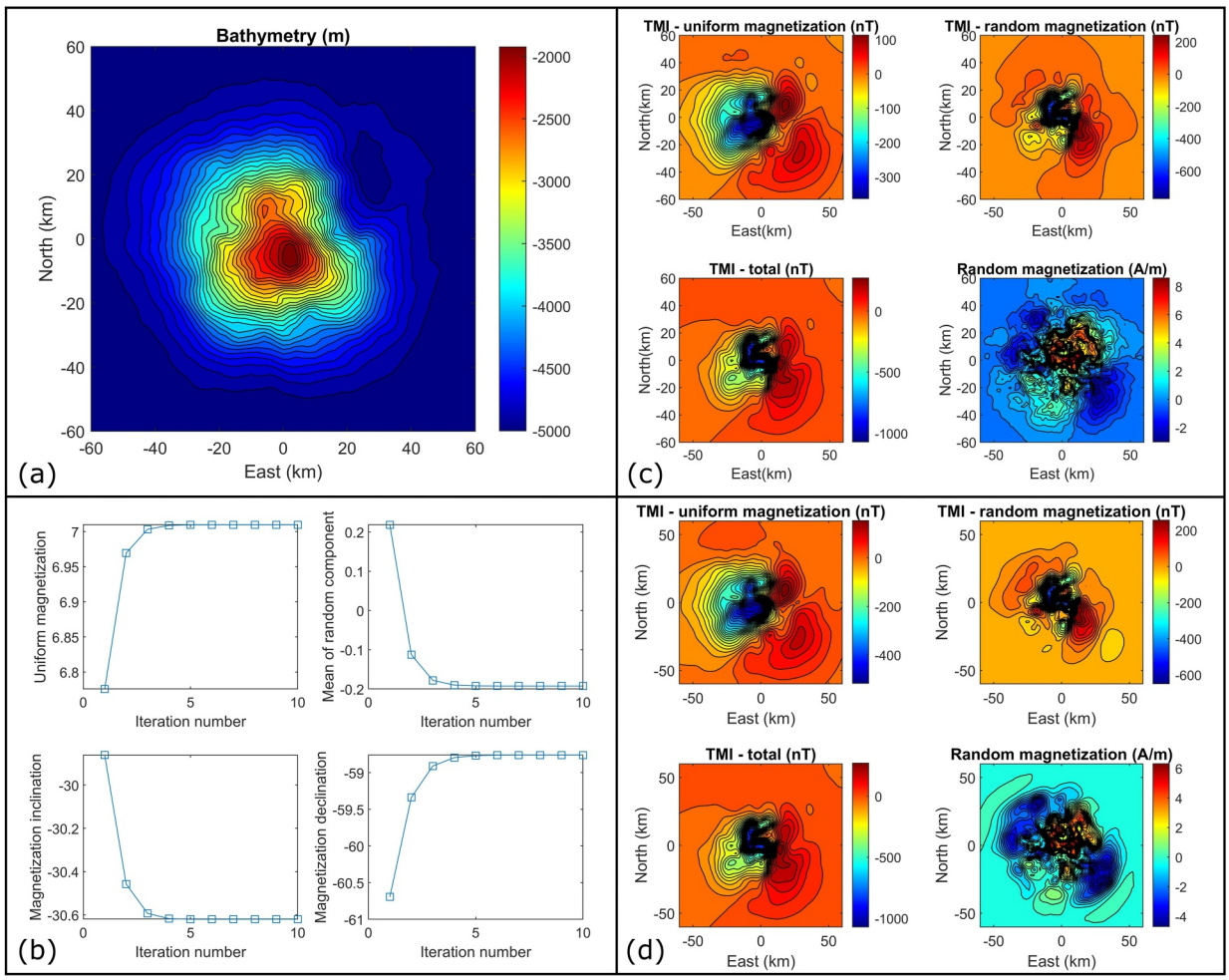

Figure 2. Example of synthetic test. The geomagnetic field direction has inclination 60° and declination 0°, whereas the true direction of the magnetization has inclination −30° and declination −60°. The seamount has a uniform magnetization component of 6 A/m in addition to the random magnetization model shown in the bottom right figure in panel (c). (a) Bathymetry model. (b) Convergence curves with changes of the different parameters at each iteration. (c) TMI—total magnetic intensity anomalies (from uniform and random magnetization models, as well as the sum of both), together with the random magnetization model. (d) Results of final inversion using a magnetization inclination of −30.6° and declination of −58.7 after the iterations shown in panel (b).

respectively. The seamount magnetization direction has inclination −30° and declination −60°. The seamount magnetization intensity is described by a uniform magnetization component of amplitude 6 A/m, combined with the zero-mean random model shown in the bottom-right plot of Figure 2c. The magnetic anomalies generated by the uniform and the random magnetization models are also shown in Figure 2c, together with the combined total magnetic intensity anomaly (TMI), generated by the superposition of both models. These subplots show that the seamount bathymetry and the corresponding magnetic anomaly are adequately sampled. These should be the main guidelines when choosing the grid size, that is, the survey extension should be large enough to enclose the seamount bathymetry from the top to the base, and to sufficiently sample the full dipolar structure of the magnetic anomaly with both negative and positive lobes.

The angular distance between the true magnetization direction and the one recovered by the algorithm can be estimated using spherical trigonometry. In particular, for two points with inclination and declination (I_1, D_1) and (I_2, D_2), the following equation

$$\cos\Delta = \sin(I_1)\sin(I_2) + \cos(I_1)\cos(I_2)\cos(D_2 - D_1), \tag{4}$$

can be used to determine the angular distance Δ between the two points.

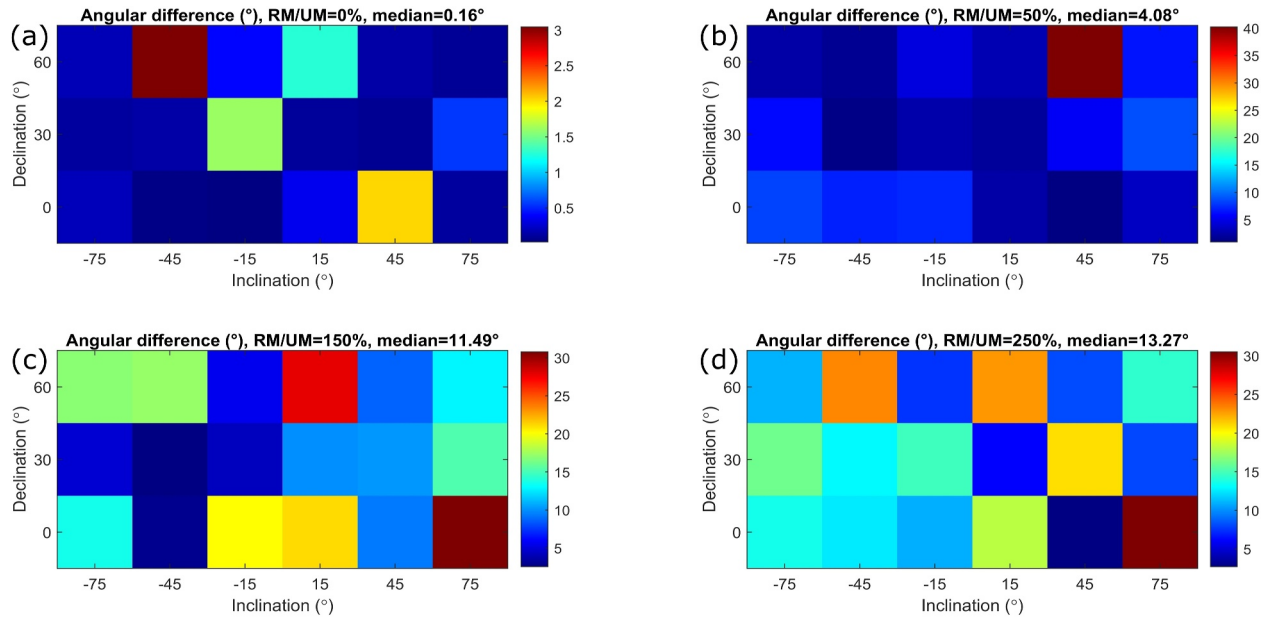

Figure 3. Angular difference in degrees between true and calculated magnetization directions, for different values of inclination and declination (a) Angular differences as a function of inclination and declination for a ratio between uniform magnetization and random magnetization RM/UM = 0%, that is, no random magnetization component. (b) Angular differences as a function of inclination and declination for a ratio between uniform magnetization and random magnetization RM/UM = 50%. (c) Angular differences as a function of inclination and declination for a ratio between uniform magnetization and random magnetization RM/UM = 150%. (d) Angular differences as a function of inclination and declination for a ratio between uniform magnetization and random magnetization RM/UM = 250%.

For the test shown in Figure 2 the algorithm has determined a uniform magnetization of ∼7 A/m, with inclination ∼−30.6° and declination of ∼−58.7°, as shown by the convergence curves in Figure 2b. These values are in good agreement with the true inclination and declination values of the seamount model, with an angular distance $\Delta \sim 1.3°$, calculated using Equation 4. At the last iteration, I carried out a final inversion to determine the random magnetization model (bottom-right plot in Figure 2d), which shows a good agreement with the true random model shown in Figure 2c. I have also shown the corresponding TMI plots (Figure 2d).

2.2. Model Tests: Effect of Random Magnetization

In this section I assess the accuracy of this method from a series of multiple synthetic tests to evaluate the response of the algorithm on known data -sets simulating morphologies of real seamounts, for different directions of the magnetization distribution as well as different intensities of the residual magnetization J^r relative to the intensity of the uniform component J^u. I have modeled random bathymetry and magnetization models as fractal noise realizations (e.g., Turcotte, 1997), following the approach described in Caratori Tontini et al. (2008). In addition to that, the seamount models are approximately centered by multiplying the bathymetry distribution for a Gaussian function peaked at the center of the survey area. The example of Figure 2 was built following these guidelines.

I analyzed the response of the algorithm in relation to variable inclination and declination values, as well as the relative importance of the amplitude of the random magnetization model compared with the intensity of the uniform magnetization model. To this aim I have generated a set of models with six inclination values equally spaced between −75° and +75°, and declination values of 0°, 30, and 60°, for a total number of 18 variable inclination and declination models, as well as four different values of the ratio of the amplitude of the random magnetization distribution (RM) and the intensity of the uniform magnetization model (UM), with RM/UM = 0%, 50%, 150%, and 250%, for a total number of 72 models. The results are shown in Figure 3, where I have plotted the angular difference between true and calculated magnetization directions.

The plots in Figure 3 do not show a clear pattern with respect to inclination and declination. The differences seem to be independent of these angular parameters. When the effect of random magnetization is absent (Figure 3a), the angular difference does not exceed 1° in the vast majority of the cases, with only one case ($I = -45°$, $D = 60°$) showing a value of ∼3°. The median in this case is ∼0.16°. However, as expected the differences increase as the effect of the random magnetization component becomes more relevant (Figures 3b–3d). The median increases from ∼4.08° to ∼13.27° as the ratio RM/UM increases from 50% to 250%. However, individual angular errors typically do not exceed 20°, with only few exceptions, such as the test in Figure 3b ($I = 45°$, $D = 60°$), or ($I = 75°$, $D = 0°$) in both Figures 3c and 3d. In these cases, this method has given a less accurate magnetization direction. However, in the remaining ∼95% of the cases the method has given good results.

2.3. Effect of Window Size

One of the possible reasons for large errors is due to the user-dependent, specific choice of a finite-size region to evaluate the truncated integrals, and whether this window is optimally centered with respect to the ideal center of the seamount. In other words, it is caused by a poor choice of the origin of the coordinate system. Ideally, the truncated integrals should be calculated using a coordinate system whose origin is horizontally located in coincidence with the horizontal components of the seamount magnetic center $\boldsymbol{r}_c$, defined as follows

$$\boldsymbol{r}_c = \frac{\int M(\boldsymbol{r})\,\boldsymbol{r}\,dV}{\int M(\boldsymbol{r})\,dV}, \tag{5}$$

where $M(\boldsymbol{r})$ is the intensity of the magnetization at a point r inside the seamount and the integration is carried out over the entire volume of the seamount.

It may be challenging to determine the position of an optimal window to carry out the integral calculations in the real case, particularly when neighboring interfering anomalies are present. I propose to use multiples windows with variable sizes and positions, to reduce the effects coming from subjective choices of these parameters. As discussed before, these windows should be large enough to enclose the seamount bathymetry from the top to the base, and to sufficiently sample the full dipolar structure of the magnetic anomaly with both negative and positive lobes.

In practice, I can achieve statistically meaningful results by using a set of variable-size, overlapping windows with centers distributed around the true magnetization center of the seamount. In this case integrated results can be obtained by averaging the single magnetization directions, that is, reducing the errors associated with a specific choice of the window to calculate the truncated integrals. Specifically, I could use the various results from the different windows as multiple realizations of the magnetization directions, and use a probability density function for these directions, such as the Fisher distribution (e.g., Butler, 2004), to determine the mean inclination and declination. Furthermore, I can assess a statistical evaluation of the dispersion of the population of directions by calculating the precision parameter k (e.g., Butler, 2004) as follows:

$$k = \frac{N-1}{N-R}, \tag{6}$$

where N is the number of windows, and R is given by

$$R = \sqrt{\left(\sum_{i=1}^{N} \cos I_i \cos D_i\right)^2 + \left(\sum_{i=1}^{N} \cos I_i \sin D_i\right)^2 + \left(\sum_{i=1}^{N} \sin I_i\right)^2}, \tag{7}$$

where I_i and D_i are the magnetization inclination and declination, respectively, determined for the generic window i. I will graphically represent the average directions and their dispersions by drawing the 95% confidence ellipse on a stereographic map (e.g., Figure 4).

Operationally I propose an initial calibration to approximate the magnetic center of the seamount by using a set of overlapping windows with variable centers and calculate the magnetization direction for each window. This magnetization direction is then used to estimate the center of a best-fitting magnetic dipole which reproduces the

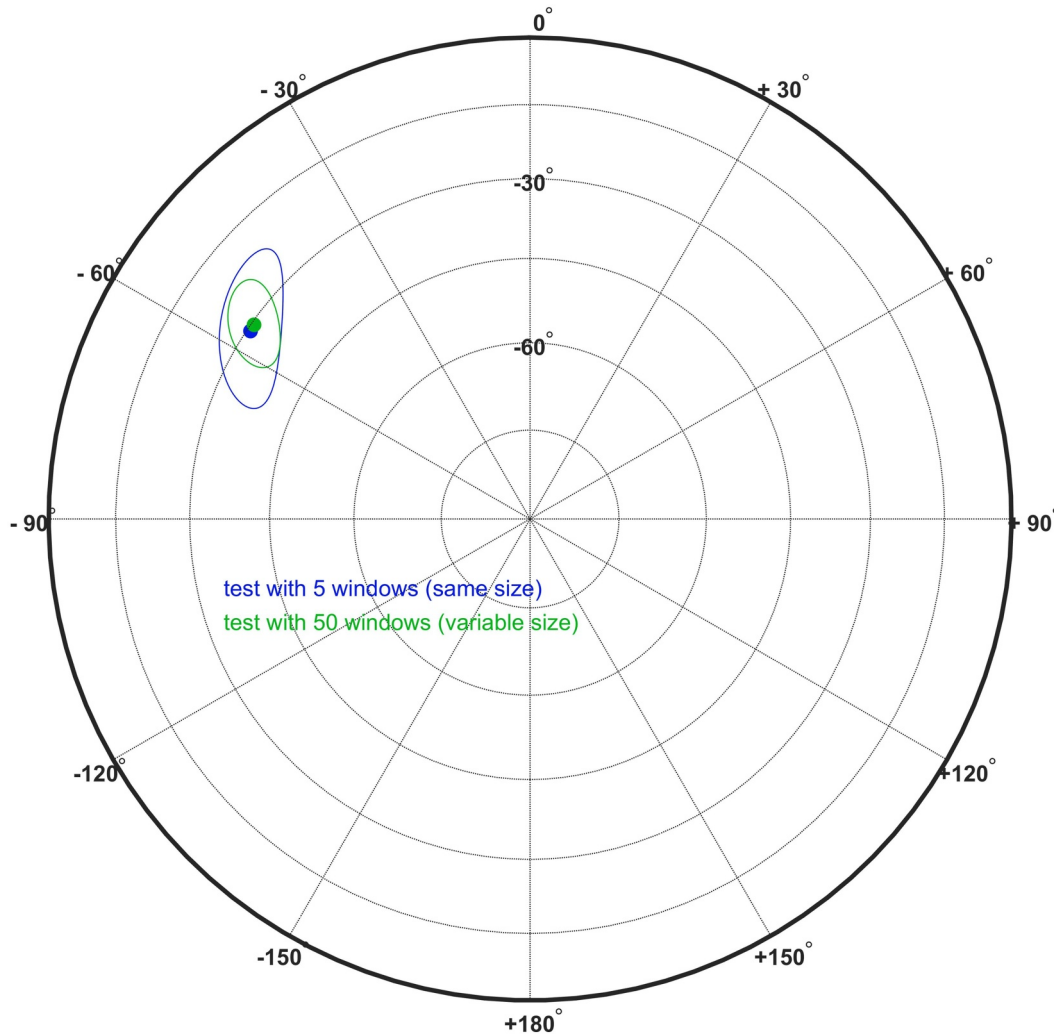

Figure 4. Results of the magnetization direction determined by using a Fisher distribution on a set of multiple overlapping windows, for the example of Figure 2. In blue I show a test based on five overlapping windows with same size, whereas in green I show the results from a set of 50 windows with variable sizes. The mean directions are represented by the colored circles, enclosed by the corresponding 95% confidence limits ellipses. Increasing the number of windows from 5 to 50 significantly increases the accuracy of the results, with the mean direction not distinguishable at the 5% significance level from the true direction with inclination I = −30° and declination $D = -60°$.

magnetic observations for each window. From these initial tests, I can calculate the arithmetic average X_c and Y_c of the horizontal coordinates of the centers and their standard deviations σ_x and σ_y. After these preliminary runs, the program is executed to determine accurate magnetization directions, by using a set of randomly generated, variable-size windows according to a 2-D Gaussian probability density centered in (X_c, Y_c), and with an isotropic standard deviation σ conservatively given by the maximum value between σ_x and σ_y. For each result the program returns the correlation coefficient r between the grid of observed magnetic anomaly O_{ij}, and the forward anomaly grid calculated using a uniform magnetization model U_{ij} as follows:

$$r = \frac{\sum_i \sum_j (O_{ij} - \overline{O})(U_{ij} - \overline{U})}{\sqrt{\left(\sum_i \sum_j (O_{ij} - \overline{O})^2\right)\left(\sum_i \sum_j (U_{ij} - \overline{U})^2\right)}}, \quad (8)$$

where $\overline{O}$ and $\overline{U}$ are the mean values of the O_{ij} and U_{ij} grids, respectively. This correlation coefficient can be used to assess the quality of the individual results. As a final step I propose to filter the set of solutions for outliers, by rejecting magnetization directions with a correlation coefficient $r < 50\%$, or when the difference between the correlation coefficient r and the mean correlation coefficient calculated from the entire set of solutions is larger than 2 standard deviations. Similarly, I reject solutions from windows centered at positions located at a distance larger than 2σ from the center (X_c, Y_c).

If the effect of the non-uniform component is strong, this method to determine the center of magnetization could fail as the solution of best-fitting magnetic dipole may not converge. If this happens, I suggest approximating the center of magnetization with the geometrical center of mass of the seamount, and then estimate the standard deviation σ from the seamount geometry and the corresponding characteristic length determined as

$$\sigma = \sqrt{\frac{A}{\pi}}, \tag{9}$$

where A is the area of the seamount summit delimited by the maximum curvature contour of bathymetry (e.g., Grosse et al., 2012).

In particular, for the example shown in Figure 2, I have applied Fisher statistics to a case where I have used five overlapping windows with same size (80% of the original size of 120 km shown in Figure 2), as well as a more articulated case with 50 overlapping windows with variable sizes (from 80% to 50% of the original size of 120 km). The results are shown in Figure 4. In both cases the true magnetization direction with inclination $I = -30°$ and declination $D = -60°$ is not distinguishable at the 5% significance level from the mean directions determined by averaging the results from multiple windows. However, as expected, by increasing the number of windows I can obtain more accurate results with smaller 95% confidence ellipses.

2.4. Practical Implementations for Real Data

The use of multiple overlapping windows is particularly useful when analyzing real data, as this allows for a statistical analysis to be implemented on multiple results. Furthermore, real data can be complicated by interfering effects of other anomalies caused by neighboring sources in proximity of the survey area. In this case the use of a smaller set of windows can be particularly effective in reducing this type of error, by isolating the local magnetic anomaly. The method is virtually insensitive to the effect of a regional field, if this can be reasonably represented by an offset in the magnetic data. This is evident by looking at the integrals in Equation 2, where adding a constant field to the magnetic data does not change the result of **M**, as this effectively results in the integration of an odd function over a symmetric domain, which is zero. Nevertheless, I recommend for any regional field, if present, to be removed by subtracting a best-fitting trend from the magnetic observations before calculating Helbig's integrals, as higher-order terms other than a constant offset could still have an impact on the calculation of the integrals.

The integrals in Equation 2 involve the use of the Cartesian components $\left(\Delta T_x, \Delta T_y, \Delta T_z\right)$ of the anomalous magnetic field caused by the seamount. These components are generally not directly measured but can be determined by phase transformations of the observed scalar magnetic anomalies (e.g., Gerovska & Araúzo-Bravo, 2006; Lourenco & Morrison, 1973; Purucker, 1990). In this case the calculation is implemented by taking the Fourier transform of the scalar total magnetic intensity anomaly ΔT:

$$\Delta T \overset{\text{FFT}}{\rightarrow} \mathcal{F}_{\Delta T}, \tag{10}$$

where $\mathcal{F}_{\Delta T}$ is the 2-D Fourier transform calculated using the Fast Fourier Transform (FFT) method (Cooley & Tukey, 1965). The Fourier transform of the field components $\mathcal{F}_{\Delta T_j}$ can be calculated by applying the following filter $\mathcal{H}_j$:

$$\mathcal{F}_{\Delta T_j} = \mathcal{H}_{\mathrm{j}} \cdot \mathcal{F}_{\Delta T}, \tag{11}$$

where the subscript $j = (x, y, z)$, and the filter $\mathcal{H}_{\mathrm{j}}$ is given by:

$$\mathcal{H}_j = \frac{D_j(k_x, k_y)}{K \sin I_F + i \cos I_F \, (k_x \cos D_F + k_y \sin D_F)}, \tag{12}$$

where:

1. k_x, k_y are the spatial wavenumber components;
2. $K = \sqrt{k_x^2 + k_y^2}$ is the modulus of the spatial wavenumber;
3. I_F and D_F are the local geomagnetic field inclination and declination, respectively;
4. i is the unit imaginary number ($i = \sqrt{-1}$);
5. $D_x(k_x, k_y) = ik_x$, $D_y(k_x, k_y) = ik_y$, and $D_z(k_x, k_y) = K$.

The magnetic field components caused by the seamount can be calculated by carrying out an inverse Fourier transform of $\mathcal{F}_{\Delta T_j}$:

$$\mathcal{F}_{\Delta T_j} \overset{\text{FFT}^{-1}}{\rightarrow} \Delta T_j. \tag{13}$$

Because the proposed method requires to calculate the Fourier transform of the observed total magnetic intensity (TMI) anomaly, I recommend adding a buffer area around the seamount by padding the magnetic anomalies beyond the limits of the seamount bathymetry, to reduce the impact of periodicity on the calculation of the Fourier transform. The use of multiple, smaller-size windows reduces the impact of interfering anomalies caused by other sources in proximity of the survey area. Furthermore, statistical analysis of the results from multiple windows is used to quantify the dispersion of the results, that is, the accuracy of the estimated mean direction. This data can be used to estimate the paleolatitude of the seamount, as well as the geographical position of the paleopoles with the associated statistical errors.

In the real case, multiple causes can generate complex magnetization distribution, such as multi-stage volcanism including recent volcanic rejuvenation, mass-wasting processes, tilting and rotation, weathering and/or alteration, including hydrothermal processes (e.g., Gee et al., 1988, 1993; Lee et al., 2003; McNutt, 1986). Furthermore, effects of Viscous Remanent Magnetization (VRM) and Induced Magnetization (IM) in the direction of the present geomagnetic field can contribute up to 15%–25% of the total seamount magnetization (Gee et al., 1989, 1993).

In addition to that, the ideal growth of a seamount should be longer that $\sim 10^5$ years to average over secular variation and use the Geocentric Axial Dipole (GAD) approximation, but care should be taken if the growth is taking place across multiple geomagnetic polarities as these may give inconsistent results (e.g., Harrison et al., 1975). I propose to use this method on selected seamounts of medium size, with little intrusive material (predominant source of VRM and IM effects), possibly less hydrothermal alteration and likely constructed within a single polarity interval, following the recommendations of Gee et al. (1993). To this aim, external information on the geological history and background of the investigated seamount is very useful to reduce potential ambiguities associated with the determination of the magnetization direction.

3. A Real Test: Ita Mai Tai

Ita Mai Tai (Figure 5) is a seamount located NW of the Marshall Islands in proximity to the Ogasawara Fracture Zone. The relationship between age and location of this seamount is controversial. Ita Mai Tai sits on Jurassic seafloor and is the southernmost of a line of four Cretaceous Guyots constituting the Magellan Seamount Trail (MST). Except for Ita Mai Tai, the other guyots (Vlider, Pako, and Ioah) provide excellent linear age progression highlighting a hot-spot origin between the Samoa, Rarotonga and Society hotspots (Koppers et al., 1998) of the South Pacific Isotopic and Thermal Anomaly (SOPITA, Smith et al., 1989).

The radiometric age of Ita Mai Tai (Koppers et al., 1998, 2003) is constrained by two samples from two different dredge sites on the N-E slope, which give an age ~118–120 Ma, which is significantly older than the other MST Guyots, implying that Ita Mai Tai volcanism is ~34–36 Myr older than expected for the MST hotspot model.

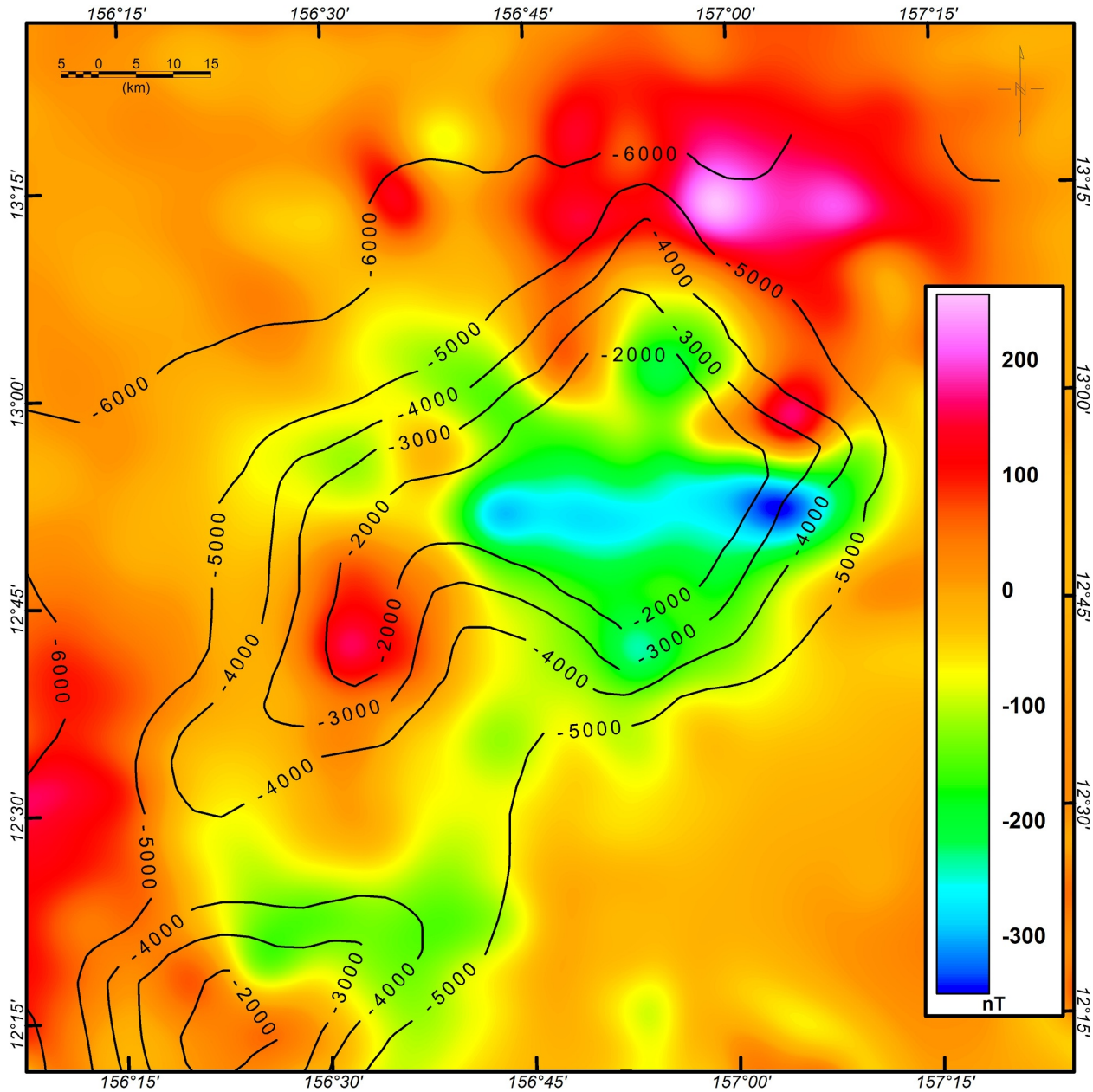

Figure 5. Ita Mai Tai magnetic anomaly and bathymetric contour lines. Data from the NOAA-NCEI archive of trackline geophysical measurements (NOAA National Geophysical Data Center, 1977), supplemented by EMAG2 data (Maus et al., 2009).

Lee et al. (2003) have analyzed shipborne marine magnetic anomalies at Ita Mai Tai using the semi-norm minimization approach of Parker et al. (1987), to estimate magnetization direction and the corresponding paleomagnetic poles. This study has shown that Ita Mai Tai has a complex morphology and magnetic anomaly pattern which reduce the accuracy of the semi-norm approach, with a low goodness of fit ratio. I have analyzed the magnetic anomaly of Ita Mai Tai, integrating data from the NOAA-NCEI archive of trackline geophysical measurements (NOAA National Geophysical Data Center, 1977), with EMAG2 data (Maus et al., 2009), to produce the magnetic grid shown in Figure 5. The magnetization directions results are obtained from a set of 86 variable-size windows centered around 156.79°E, 12.827°N with $\sigma \sim 2$ km, with sizes in the range [95–110] km, following the guidelines described in Section 2.3. The average magnetization inclination for Ita Mai Tai is $I = -41.7°$ and average declination is $D = 9.0°$, with the 95% confidence ellipse shown in Figure 6.

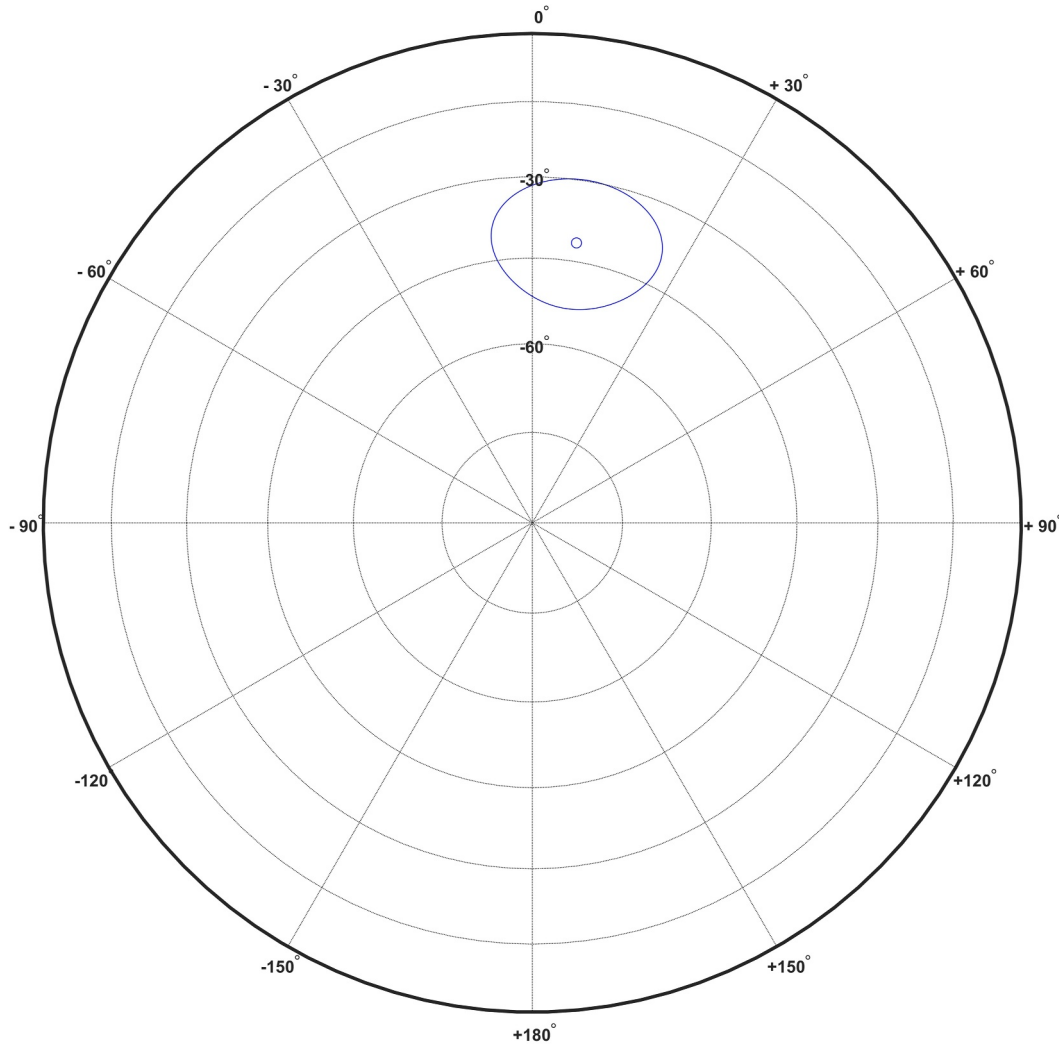

Figure 6. Ita Mai Tai magnetization direction.

The magnetization direction obtained by Lee et al. (2003) using a semi-norm minimization is characterized by an inclination $I = -58°$ and declination $D = 25.3°$, which in turn corresponds to a paleomagnetic pole for Ita Mai Tai with coordinates 313.9°E, 32.5°N, which departs substantially from the APWP (Sager, 2007) of the Pacific plate (Figure 7). The corresponding paleomagnetic pole using my method lies at 324.3°E, 52.2°N. This falls remarkably close to the ∼120 Ma pole for the Pacific plate (Figure 7), showing a result more consistent with the radiometric age samples giving an average age of ∼118–120 Ma (Koppers et al., 1998, 2003).

4. The Rano Rahi Seamount Province

4.1. Geological and Geophysical Studies

I carried out a detailed study of the magnetization directions of the off-axis submarine volcanoes located west of the East Pacific Rise (EPR), between 17°S and 19°S (Figure 8) to determine a magnetic chronology of this region. The west flank of the EPR here is characterized by many off-axis seamounts, which are part of the Rano Rahi Seamount Province (Scheirer et al., 1995) extending from 15°S to 19°S.

This segment if the EPR is characterized by superfast asymmetric spreading up to ∼150 mm/yr, with two distinct seamount chains directions, parallel to either relative plate motion or absolute plate motion, respectively (Sinton et al., 1991). Acoustic backscatter in this region indicates that the easternmost ends of the seamount chains are characterized by high reflectivity, indicating active volcanism with recent lava flows up to 60–80 km from

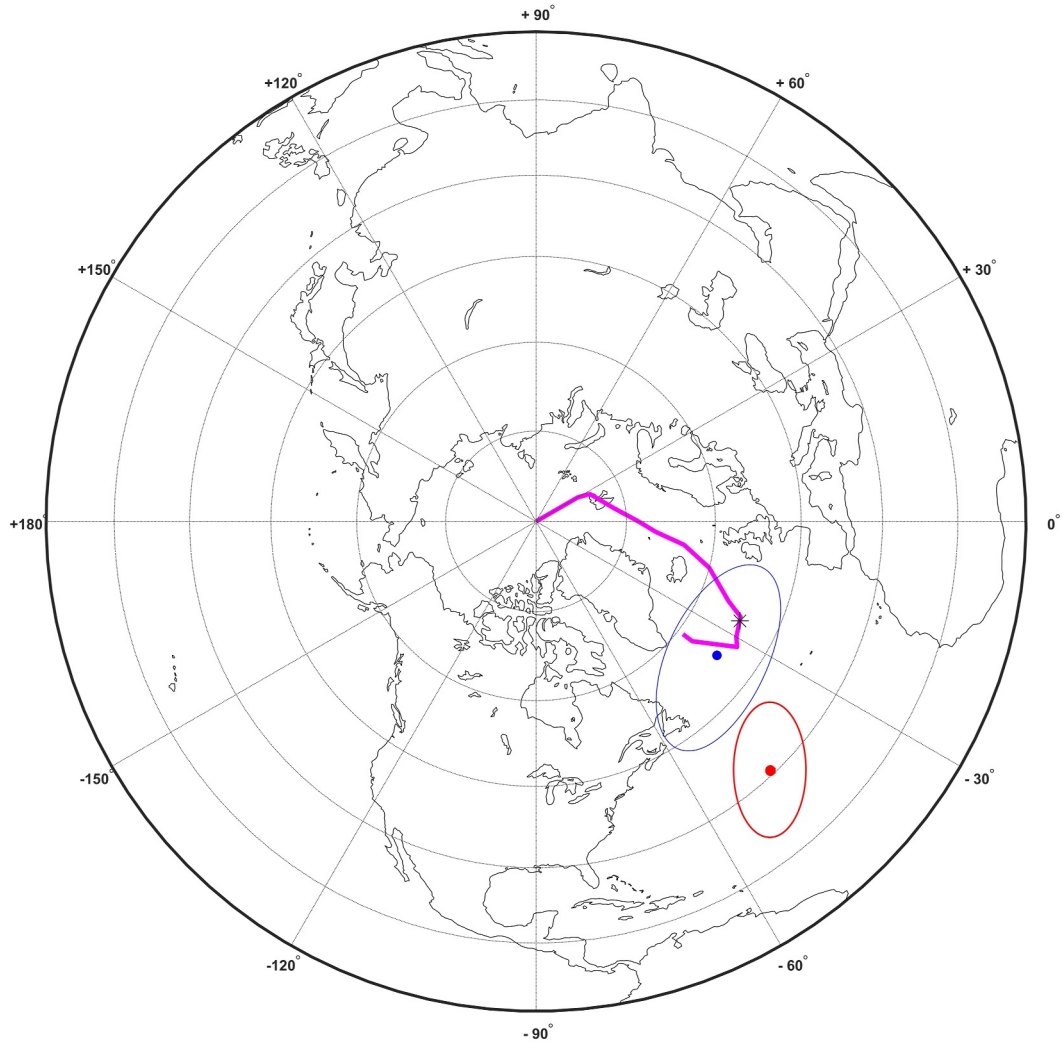

Figure 7. Ita Mai Tai paleomagnetic poles from semi-norm minimization (red ellipse, re-drawn from Lee et al., 2003), and my method (blue ellipse). The magenta line shows the Pacific APWP (Sager, 2007). The black asterisk shows the position of the ~120-Ma pole, that is, the radiometric age of the Ita Mai Tai samples.

spreading axis (Shen et al., 1993; Sinton et al., 2002), implying that these seamounts could be significantly younger than the oceanic crust they sit on (White et al., 1998). Several seamount chains, 25–140 km long, are identified in this region (Figure 8), extending westward up to ages of ~6.5 Ma (Scheirer et al., 1995). The first magnetic studies in this region have shown that long seamount chains are characterized by different magnetic polarities, indicating a progressive temporal origin for these chains, with the vast majority of seamounts being formed within 25 km of the ridge axis (Scheirer et al., 1995).

This region shows many more seamounts compared for example, to the North East Pacific Rise (NEPR) 8°–17°N (Romano et al., 2022), and volume estimates indicate that up to ~2% of volcanic material is extruded off-axis at these seamounts (Shen et al., 1993). The MELT experiment, based on a tomographic inversion of seismic refraction data (Bazin et al., 1998), has shown a broad symmetric region of melt production and faster upwelling under the Rano Rahi Seamount Field, indicating melt production up to 100 km from the ridge axis, likely responsible for the creation of the corresponding off-axis seamounts and lava flows (Scheirer et al., 1998).

Hall et al. (2006) have carried out radiometric dating by ^{40}Ar-^{39}Ar incremental heating from several samples from the Rano Rahi Seamount Field. Their results confirm a superfast and asymmetric spreading and abundant magma supply and maximum melt production on the Pacific Plate west of the EPR axis to explain the unusual large number of seamounts in this region.

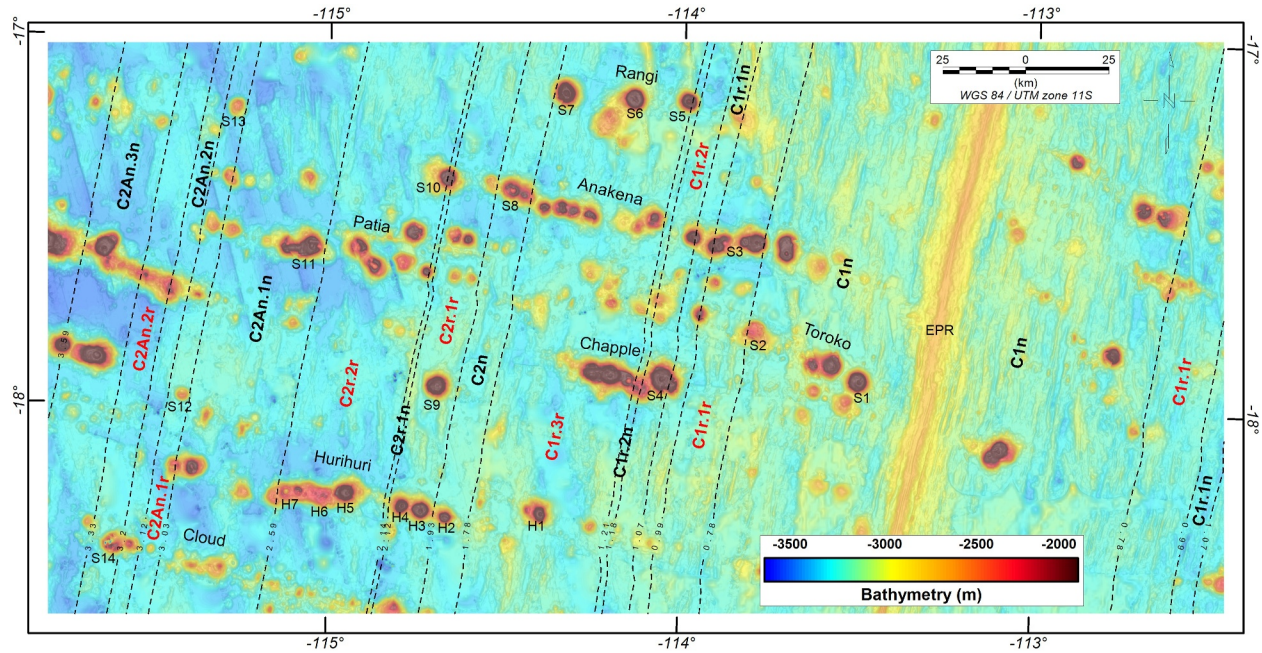

Figure 8. Bathymetry of the west flank of the EPR 17°–19°S. The intervals of seafloor age (Ma) are shown by dashed lines, following the magnetic chron nomenclature of Cande and Kent (1995), with black labels for normal polarities and red labels for reversed polarities. Submarine volcanoes from different chains (Toroko, Chapple, Anakena, Rangi, Patia and Cloud) are identified by labels S1–S14, and labels H1–H7 for the Hurihuri chain. Bathymetry data from Global Multi-Resolution Topography (GMRT) compilation (Ryan et al., 2009) downloaded using GeoMapApp (www.geomapapp.org).

4.2. Bathymetry and Magnetic Data

The bathymetry data used for the analysis of the Rano Rahi seamounts were extracted from the Global Multi-Resolution Topography (GMRT) compilation (Ryan et al., 2009). These data were re-gridded to a spatial resolution of 250 m (Figure 8). I extracted the magnetic data from the Marine Trackline Geophysical Database of NOAA (NOAA National Geophysical Data Center, 1977). These line data were analysed and corrected for spikes or other possible measurement errors and leveled using intersection errors to reduce differences coming from the relative baselines of the different surveys. These line-data were gridded using a minimum curvature algorithm with a spatial resolution of 250 m and co-registered with the bathymetry grid (Figure 9).

I selected two subsets of seamounts to carry out the magnetization direction analysis. Fourteen seamounts are selected from different chains (Toroko, Chapple, Anakena, Rangi, Patia, and Cloud) and are named S1–S14 (numbers increasing westward, toward older seafloor ages). Furthermore, I have selected seven seamounts that can be attributed to the same Hurihuri chain, named H1–H7 (numbers increasing westward, toward older seafloor ages). Square grids enclosing each of S1–S14 and H1–H7 seamount were then extracted for the magnetization direction analysis. For each seamount I carried out a preliminary optimization for the center of magnetization (Section 2.3), and then magnetization directions were obtained using a set of 80–100 randomly generated overlapping variable-size windows, with sizes in the range of 75%–60% of the original square grids, fully characterizing the seamount bathymetry and the complex magnetic anomaly pattern of each seamount. Magnetic polarities are determined from the positions of the 95% confidence ellipses, that is, given the magnetic latitude of the Rano Rahi Seamount Field, negative inclinations with declinations in the range [−90°; 90°] are interpreted as normal polarities, whereas positive inclinations with declinations in the range [90°; 270°] are interpreted as reverse polarities. The algorithm gave reliable results with well-defined polarities for each chosen seamount.

I use the magnetic polarity nomenclature and ages of Cande and Kent (1995), where magnetic chrons and subchrons are indicated with their polarities with letter r (reverse) or n (normal), respectively, at the end of their names (e.g., Ogg, 2020). The closest magnetic chron with similar polarity and age less or equal to the age of the seafloor can be attributed unambiguously to each seamount. Since volcanoes can form up to 80 km off-axis (Shen et al., 1993; Sinton et al., 2002), I chose to attribute 2 magnetic chrons with same polarity to those seamounts where magnetic chron ages of same polarities fall within 80 km of the underlying seafloor age. In addition to these

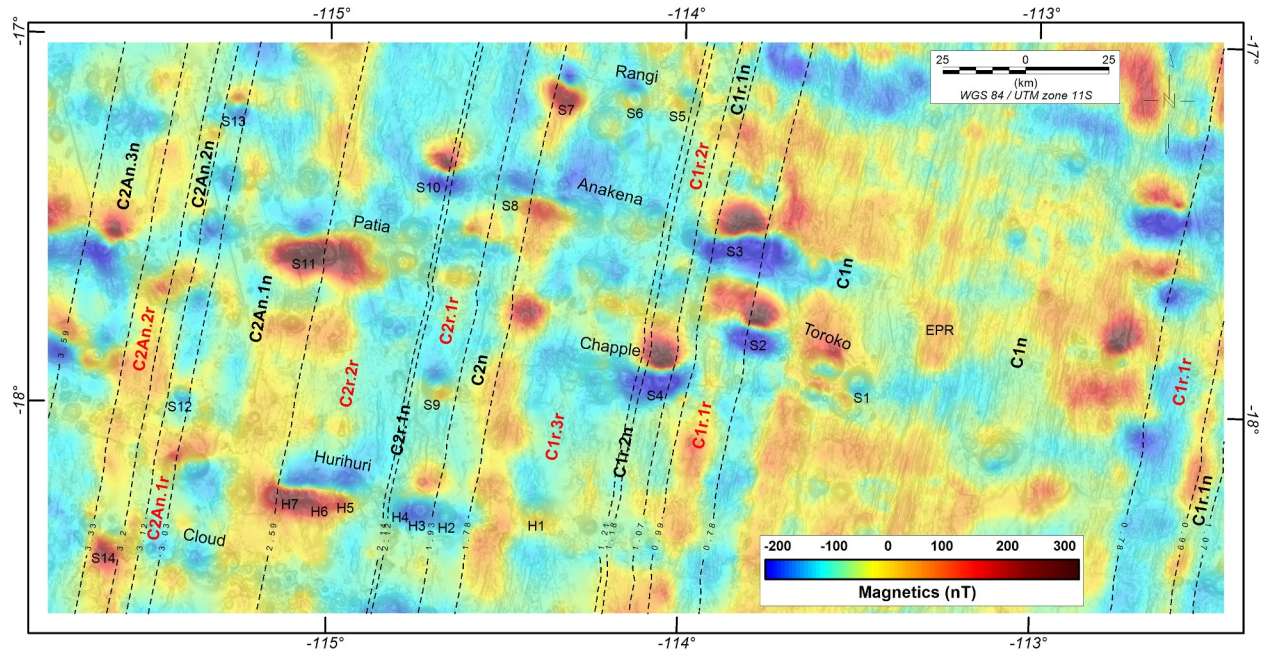

Figure 9. Magnetic anomalies of the west flank of the EPR 17°–19°S, with shaded relief of the bathymetry in Figure 8. Same nomenclature of Figure 8 for the age of the seafloor, seamount and chains, and magnetic chrons. Magnetic data from the Marine Trackline Geophysical Database of NOAA (NOAA National Geophysical Data Center, 1977).

data, I have used two radiometric ages to constrain the magnetic chronology. These data come from Hall et al. (2006) for seamounts S4 on the Chapple chain and S10 on the Anakena chain, respectively (Figure 8).

5. Results

5.1. Magnetization Directions, Polarities and Magnetic Chrons

I will present the results of the analysis of magnetization directions separately for seamounts S1–S14 and H1–H7. This is because seamounts H1–H7 can be attributed to the same chain (Hurihuri) and for this reason they can provide a more consistent assessment of magnetic age progression. The magnetization results (Figure 10) show a pattern of alternating normal and reverse polarities with a westward progression consistent with the intervals of the geomagnetic polarity time scale. Some seamounts (S3, S4, S5, S8, S10, S11, S12, S13) show magnetic polarities opposite to their underlying seafloor, indicating off-axis formation. The result for S5 shows a large 95% confidence ellipse, indicating a poor accuracy of my method. Since S5 is located at the boundary of two seafloor ages of opposite polarities (chrons C1r.3r and C1r.2n in Figure 8), it is possible that the magnetization of this seamount could be acquired across different chrons, inducing a less accurate result. Similar considerations apply to S8, which is characterized by an anomalous declination ~90°. I could attribute well-defined magnetic chrons to S1, S2, S3, S12, and S13. Figure 10 shows that magnetization directions roughly cluster at opposite polarities, with a slight westward shift (~20°) of the magnetic declination.

Seamounts H1–H7 can be attributed to the same chain (Hurihuri). This may reduce the ambiguity in the determination of the magnetic chrons from the magnetization directions, if I assume a progressive age of formation of the seamount from the westernmost H7 (oldest) to the easternmost H1 (youngest). The corresponding results are shown in Figure 11, where well-defined magnetic chrons have been attributed to each seamount.

Except for seamounts H3 and H4, all the other seamounts have the same polarities of their underlying seafloor. Furthermore, the size of the 95% confidence ellipses for these seamounts show a good accuracy for the calculated magnetization directions.

I summarize these results in Figure 12, where I show the ages corresponding to the determined magnetic chrons for seamounts S1–S14 and H1–H7, and their relation to the seafloor ages and the radiometric ages for S4 and S10.

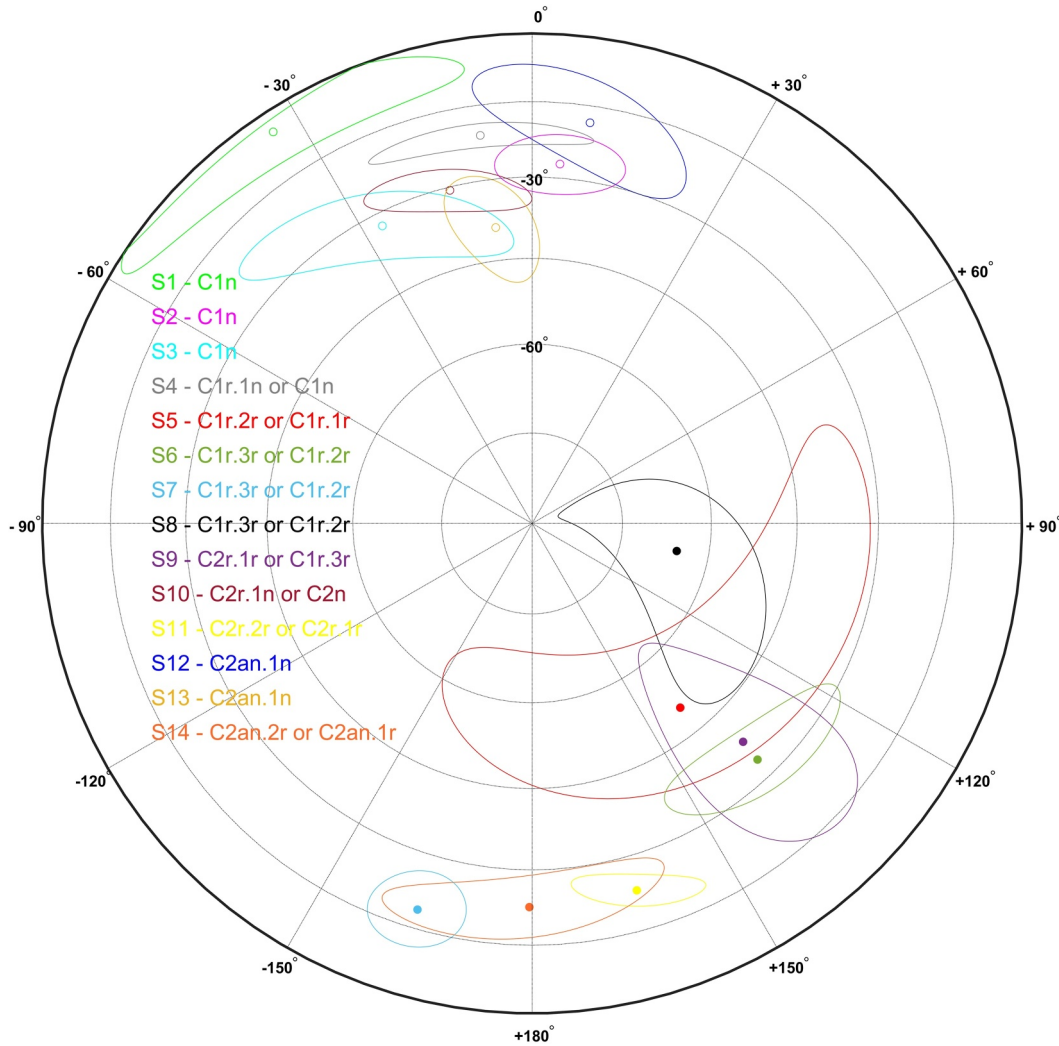

Figure 10. Magnetization directions for Seamount S1–S14, with corresponding magnetic chrons. Empty circles show negative inclinations, whereas full circles show positive inclinations.

6. Discussion

The magnetization directions determined for the set of seamounts S1–S14 and H1–H7 of the Rano Rahi Seamount Field show a resulting pattern of normal and reverse polarities at progressive distances from the EPR ridge which is consistent with the magnetic polarity time-scale in the interval 0–3 Ma (Figure 13). Ages of seamounts generally show a westward increase, with some exception if I consider the ambiguities in chron interpretation. For example, if I attribute chron C1r.1n to S4 and C1r.1r to S5, then S5 is younger than S4 despite being located at further distance from the EPR ridge. This is possible considering that Rano Rahi seamounts can form up to 80 km from the EPR ridge and would confirm the existence of an off-axis lithospheric control on the emplacement of the Rano Rahi seamounts. Except for less accurate polarities determined for S5 and S8 as discussed before, the investigated seamounts show well-defined magnetic polarities. Rock magnetization of submarine volcanoes can be acquired at different times spanning multiple magnetic polarities. If the time of formation of a submarine volcano is long, then I would expect a complex magnetic pattern characteristic of multiple polarity reversals. However, observations at Rano Rahi Seamount Field indicate that the well-defined pattern of polarities can be explained if the time-scales of seamount growth are shorter than the average time-scales of magnetic polarity intervals.

In particular, S1–S3 show well-defined normal polarities. Being located on seafloor age <~1 Ma, their normal polarity can be unambiguously attributed to chron C1n (<0.78 Ma). The normal polarity of S4 could be attributed

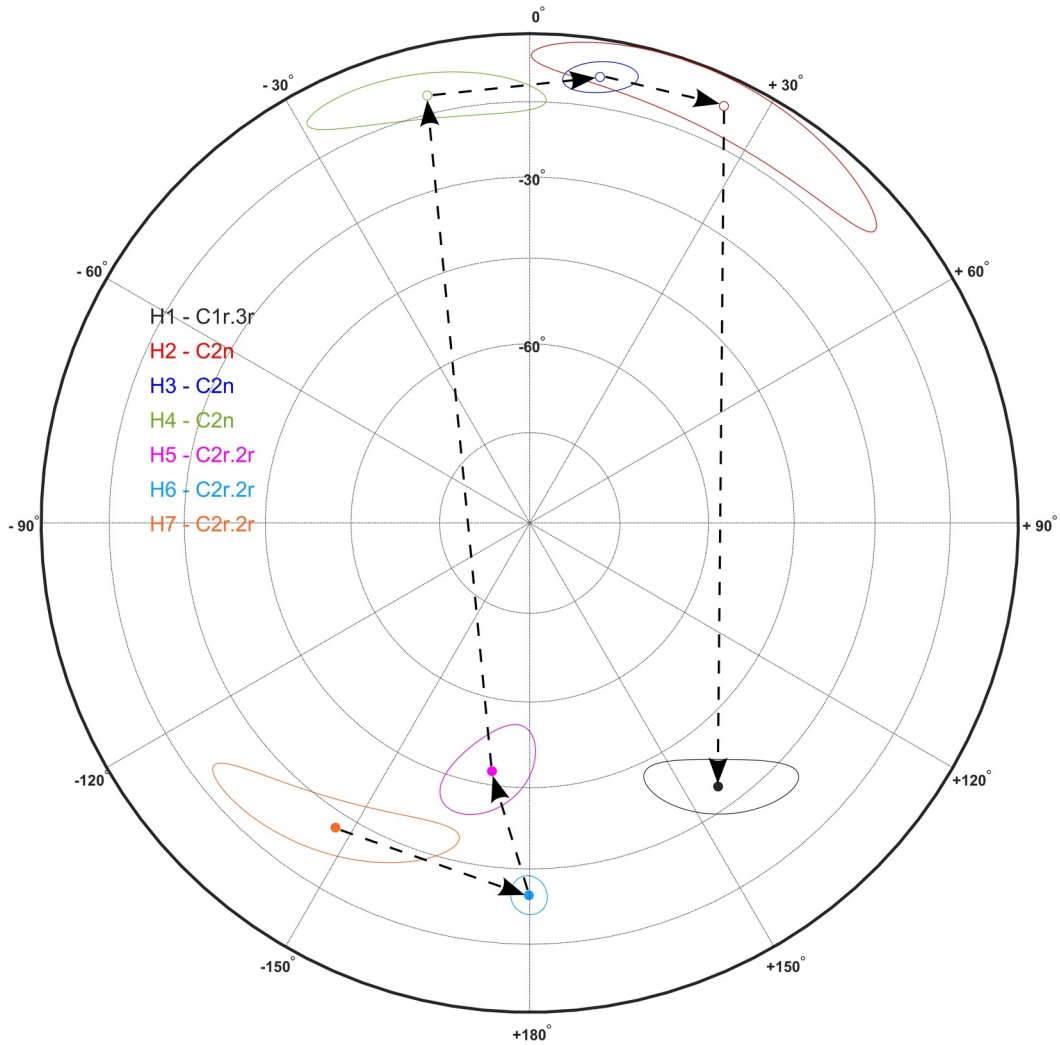

Figure 11. Magnetization directions for Seamount H1–H7 (Hurihuri chain), with corresponding magnetic chrons. Empty circles show negative inclinations, whereas full circles show positive inclinations. Arrows indicate the age progression from oldest (H7) to youngest (H1).

to either C1r.1n or C1n. Here, radiometric dating shows an age of ∼0.96 Ma, suggesting that C1r.1n could be the more likely chron. However, radiometric dating only samples the more recent seafloor and may not be fully representative of the history of formation. Seamounts S5–S9 show clear reverse polarities. Seamount S5 is located on seafloor with age crossing the boundary between two different polarities, which may explain the less accurate magnetization directions. Seamounts S6 and S7, on the Rangi chain, are both located on seafloor of reverse polarity (C1r.3r). For this reason, the most obvious explanation for their observed reverse polarities would be to attribute the same chron C1r.3r to these seamounts. However, I cannot exclude chron C1r.2r, which would imply an off-axis formation of up to ∼50 km away from the EPR ridge for S7 and up to ∼30 km for S6, respectively. The same applies to S8, implying an off-axis formation in the range [10–80] km away from the EPR ridge. The remaining seamounts S10–S14 show an alternate pattern of polarities, likely a reflection of the short length of polarity intervals between ∼2.0 and ∼3.5 Ma. For S10 a radiometric age of ∼1.83 Ma exist, which could then unambiguously attribute this seamount to chron C2n (1.78–1.93 Ma).

The interpretation of seamounts H1-H7 is less ambiguous if I attribute them to the same Hurihuri chain. Even if these seamounts were formed off-axis, their westward age progression is likely to be respected, from H1 (youngest) to H7 (oldest), with differences in ages comparable to the differences in ages of their underlying seafloor. I can unambiguously attribute a magnetic chron C2n to the normal polarities observed for H2, H3, and

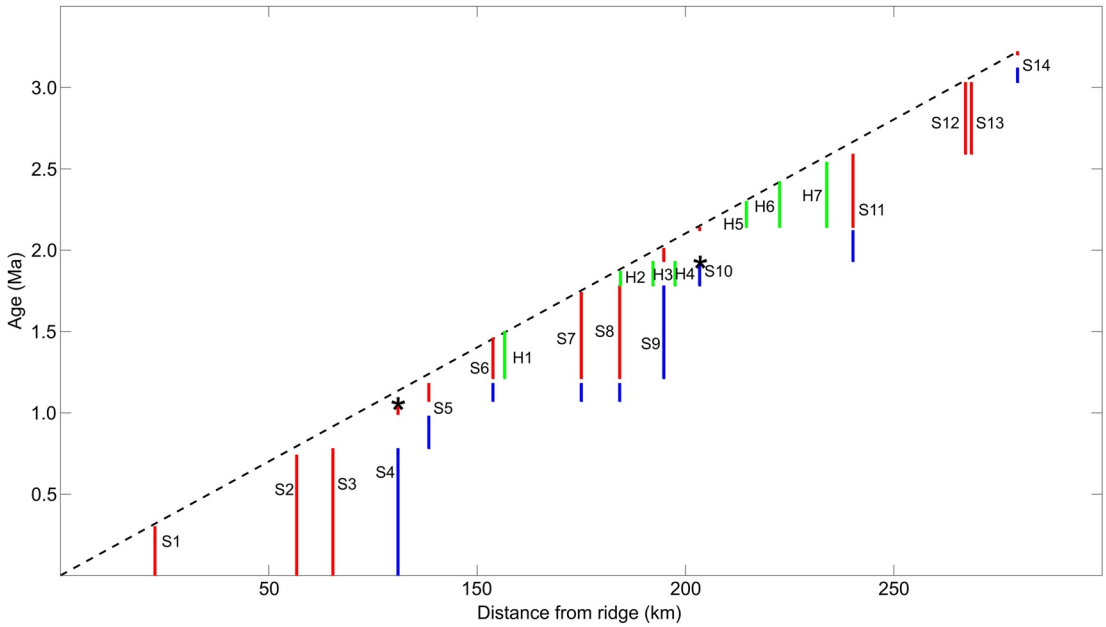

Figure 12. Seamount ages inferred from magnetic chrons and polarities as a function of distance from the ridge axis. I have attributed two possible chrons to seamounts S4, S5, S6, S7, S8, S9, S10, S11, and S14, which exhibit two possible ages indicated by the red and blue bars, respectively. The black asterisks indicate the radiometric ages available for S4 and S10. The green bars indicate the ages of seamounts H1–H7, which are unambiguously determined. The dashed black line is the seafloor age.

H4, as the other interval of C1r.2n looks too short to accommodate a spatial distance of ∼20 km between H2 and H4 at a spreading rate of ∼150 mm/yr. I can attribute chron C1r.3r to H1 and C2r.2r to H5, H6, and H7. This implies a chron progression for these Hurihuri chain seamounts shown in Figure 11, with ages from ∼1.21 (min age of C1r.3r) to 2.59 Ma (max age of C2r.2r). If this progression is representative of a hot-spot type motion, where volcanoes form at the same spot while the underlying plate moves, a distance of ∼85 km between H1 and

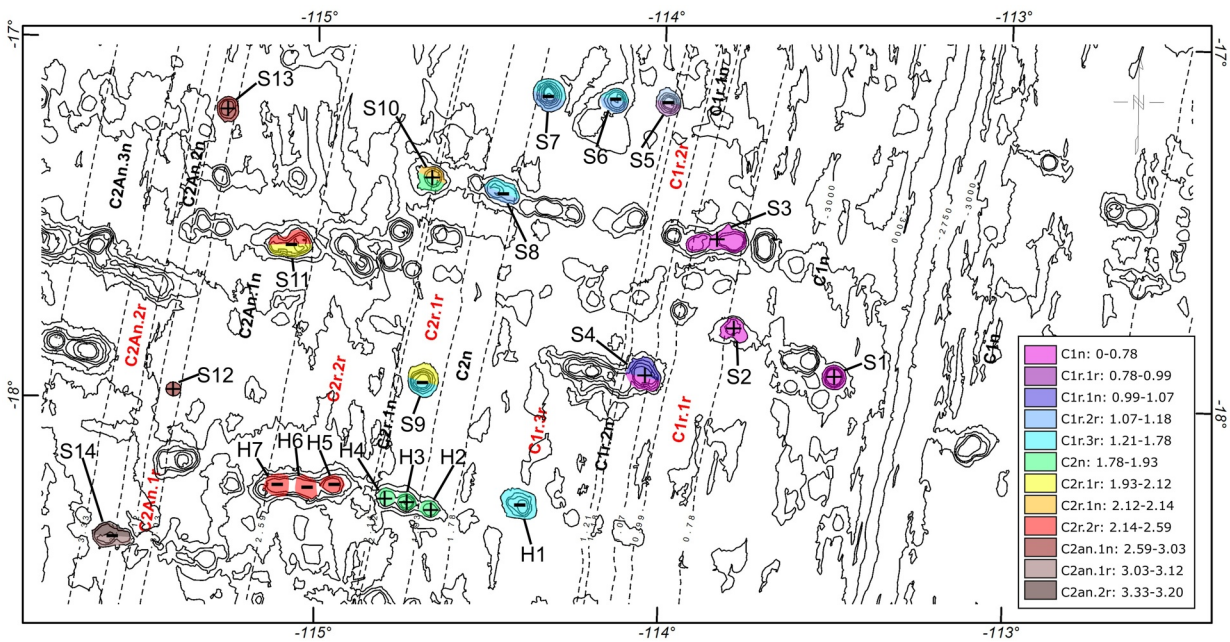

Figure 13. Seamount chrons from interpretation of magnetic polarities over bathymetry contour. Symbol + and – indicate normal or reverse polarities, respectively. When chron ambiguities exist, volcanoes are colored with two colors, with the oldest chron up. The color table shows magnetic chrons and age intervals (Ma) from Cande and Kent (1995). Same nomenclature of Figure 8 for the age of the seafloor, seamount names, and seafloor magnetic chrons.

H7 would imply a spreading rate of ∼123 mm/yr, which is not too different than the actual value of ∼150 mm/yr, considering the uncertainties associated with the exact times of formation of these seamounts, which can only be determined within the resolution of the corresponding magnetic polarity intervals.

I can calculate constructional volume rate R_V, for a single seamount, as follows:

$$R_V = \frac{V_s}{\Delta T}, \tag{14}$$

where V_s is the seamount volume and ΔT is the time-span required to build the seamount obtained from the ages of magnetic polarity intervals (Figure 12). I can estimate conservative values for the volume rates of the investigated seamounts. In addition to H1–H7, I have attributed unambiguous polarities to S1, S2, S3, S12, and S13. By using Equation 14 on the subset of seamounts H1–H7 along the Hurihuri chain, I obtain an average constructional volume rate $R_V = 0.7 \times 10^{-3} \pm 0.4 \times 10^{-3}$ km^3/yr, where the uncertainty is estimated from the standard deviation. By including seamounts S1, S2, S3, S12 and S13, I obtain an average constructional volume rate $R_V = 0.5 \times 10^{-3} \pm 0.4 \times 10^{-3}$ km^3/yr. I can include all the seamounts in the calculation, and estimate extreme values of the constructional volume rates, by applying Equation 14 separately to minimum and maximum ages, respectively. This gives a possible maximum rate of $1.3 \times 10^{-3} \pm 1.8 \times 10^{-3}$ km^3/yr, and minimum rate of $0.5 \times 10^{-3} \pm 0.4 \times 10^{-3}$ km^3/yr. These results suggest that the real constructional volume rate is likely in the range 0.5×10^{-3}–1.3×10^{-3} km^3/yr.

Assuming a conservative approach where these volcanoes have been built during the entire length of a polarity interval, the average chron duration is in the range 0.2–0.4 Myr, and I can assume this as an average order of magnitude for the timespan required to build one of these volcanoes. This places a limit on the applicability of this method. The spreading rates and constructional volume rates should be reasonably fast to guarantee that seamounts are built within a well-determined magnetic polarity event, that is, the average time-span to build a seamount should be less than 0.2–0.4 Myr. Slower volume rates will cause the average time-span to build a seamount to go across multiple magnetic polarity intervals, producing inaccurate ages.

Considering an approximate magma supply rate of ∼21 km^3/yr at mid-ocean ridges (Crisp, 1984), then the 17°–19°S segment of the EPR contributes for $\sim 5.0 \times 10^{-2}$ km^3/yr. This implies that during its activity each submarine volcano of the Rano Rahi Seamount Field has accounted for approximately 1% and 2% of the yearly magma supply rate of the corresponding segment of the EPR, which becomes a significant component considering the large number of seamounts in this region.

7. Conclusion

I have proposed a method to determine the magnetization directions of isolated seamounts, based on the use of Helbig's integrals constrained by the seamount morphology. The method has proven successful on a set of synthetic tests and a well-constrained real data set from Ita Mai Tai in the Magellan Seamount Trail.

The systematic application of the proposed method to the Rano Rahi Seamount Field has shown that these submarine volcanoes show clear magnetic polarities. The average magnetization of these seamounts is the expression of their main constructional episodes, implying that their growth was fast enough to occupy single magnetic polarity intervals. Given the ages and volumes of these volcanoes, I have found an average constructional rate in the range 0.5×10^{-3}–1.3×10^{-3} km^3/yr for each volcano. However, these are conservative rates, that is, likely provide minimum values of average constructional rates given the temporal resolution of geomagnetic polarity intervals, implying that off-axis seamounts of the Rano Rahi Field provide a significant contribution to the total magma output of the 17°–19°S segment of the EPR.

Data Availability Statement

Datafiles for the seamounts of the Rano Rahi Seamount Field and the software to carry out the magnetization direction analysis and generate synthetic models of bathymetry and magnetization are available at https://doi.org/10.5281/zenodo.14016363 (Caratori Tontini, 2024). Bathymetry data from Global Multi-Resolution Topography (GMRT) compilation (Ryan et al., 2009) and magnetic data from the Marine Trackline Geophysical Database of

NOAA (NOAA National Geophysical Data Center, 1977) were downloaded using GeoMapApp (www.geomapapp.org).

Acknowledgments
I would like to thank the Associate Editor Colin Farquharson and the reviewers Jyun-Nai Wu and Valeria Cristina Ferreira Barbosa for their comments which improved the level of this manuscript. This study was supported by University of Genova Research Funds—Fondi di Ricerca di Ateneo (FRA2023). Open access publishing facilitated by Universita degli Studi di Genova, as part of the Wiley - CRUI-CARE agreement.

References

Acton, G. D., & Gordon, R. G. (1991). A 65 Ma palaeomagnetic pole for the Pacific plate from the skewness of magnetic anomalies 27r-31. *Geophysical Journal International*, *106*(2), 407–420. https://doi.org/10.1111/j.1365-246X.1991.tb03904.x

Bazin, S., van Avendonk, H., Harding, A. J., Orcutt, J. A., Canales, J. P., Detrick, R. S., & MELT Group. (1998). Crustal structure of the flanks of the East Pacific Rise: Implications for overlapping spreading centers. *Geophysical Research Letters*, *25*(12), 2213–2216. https://doi.org/10.1029/98gl51590

Butler, R. F. (2004). Paleomagnetism: Magnetic domains to geologic terranes (Electronic Edition, p. 238).

Cande, S. C., & Kent, D. V. (1995). Revised calibration of the geomagnetic polarity timescale for the Late Cretaceous and Cenozoic. *Journal of Geophysical Research*, *93*(B4), 6093–6095. https://doi.org/10.1029/94jb03098

Caratori Tontini, F. (2024). Software and dataset supporting paper "Seamount magnetism from Helbig's integrals: Application to the Rano Rahi Seamount Field (East Pacific Rise 17°–19°S)", Journal of Geophysical Research (2025), by Fabio Caratori Tontini. In Seamount magnetism from Helbig's integrals: Application to the Rano Rahi Seamount Field (East Pacific Rise 17°–19°S) (Version v2) [Software]. *Zenodo*. https://doi.org/10.5281/zenodo.14016363

Caratori Tontini, F., Cocchi, L., & Carmisciano, C. (2008). Potential-field inversion for a layer with uneven thickness: The Tyrrhenian Sea density model. *Physics of the Earth and Planetary Interiors*, *166*(1–2), 105–111. https://doi.org/10.1016/j.pepi.2007.10.007

Caratori Tontini, F., & Pedersen, L. B. (2008). Interpreting magnetic data by integral moments. *Geophysical Journal International*, *174*(3), 815–824. https://doi.org/10.1111/j.1365-246X.2008.03872.x

Clark, D. A. (2014). Methods for determining remanent and total magnetisations of magnetic sources—A review. *Exploration Geophysics*, *45*(4), 271–304. https://doi.org/10.1071/eg14013

Cooley, J. W., & Tukey, J. W. (1965). An algorithm for the machine calculation of complex Fourier series. *Mathematics of Computation*, *19*(90), 297–301. https://doi.org/10.1090/s0025-5718-1965-0178586-1

Cottrell, R. D., & Tarduno, J. A. (2000). Late Cretaceous true polar wander: Not so fast. *Science*, *288*(5475), 2283–2287. https://doi.org/10.1126/science.288.5475.2283a

Crisp, J. A. (1984). Rates of magma emplacement and volcanic output. *Journal of Volcanology and Geothermal Research*, *20*(3–4), 177–211. https://doi.org/10.1016/0377-0273(84)90039-8

Gee, J., Staudigel, H., & Tauxe, L. (1989). Contribution of induced magnetization to magnetization of seamounts. *Nature*, *342*(6246), 170–173. https://doi.org/10.1038/342170a0

Gee, J., Staudigel, H., Tauxe, L., Pick, T., & Gallet, Y. (1993). Magnetization of the La Palma seamount series: Implication for seamount paleopoles. *Journal of Geophysical Research*, *98*(B7), 11743–11767. https://doi.org/10.1029/93jb00932

Gee, J., Tauxe, L., Hildebrand, A., Staudigel, H., & Lonsdale, P. (1998). Nonuniform magnetization of Jasper Seamount. *Journal of Geophysical Research*, *93*(B10), 12159–12175. https://doi.org/10.1029/JB093IB10p12159

Gee, J., Tauxe, L., Hildebrand, J. A., Staudigel, H., & Lonsdale, P. (1988). Nonuniform magnetization of Jasper Seamount. *Journal of Geophysical Research*, *93*(B10), 12159–12175. https://doi.org/10.1029/jb093ib10p12159

Gerovska, D., & Araúzo-Bravo, M. J. (2006). Calculation of magnitude magnetic transforms with high centricity and low dependence on the magnetization vector direction. *Geophysics*, *71*(5), 121–130. https://doi.org/10.1190/1.2335516

Grosse, P., van Wyk de Vries, B., Euillades, P., Kervyn, M., & Petrinovic, I. A. (2012). Systematic morphometric characterization of volcanic edifices using digital elevation models. *Geomorphology*, *136*(1), 114–131. https://doi.org/10.1016/j.geomorph.2011.06.001

Hall, L. S., Mahoney, J. J., Sinton, J. M., & Duncan, R. A. (2006). Spatial and temporal distribution of a C-like astenospheric component in the Rano Rahi Seamount Field, East Pacific Rise, 15°–19°S. *Geochemistry, Geophysics, Geosystems*, *7*(3), Q03009. https://doi.org/10.1029/2005GC000994

Harrison, C. G. A., Jarrard, R. D., Vacquier, V., & Larson, R. L. (1975). Paleomagnetism of Cretaceous Pacific Seamounts. *Geophysical Journal of the Royal Astronomical Society*, *42*(3), 859–882. https://doi.org/10.1111/j.1365-246x.1975.tb06455.x

Helbig, K. (1963). Some integrals of magnetic anomalies and their relation to the parameters of the disturbing body. *Zeitschrift für Geophysik*, *29*, 81–96.

Koppers, A. A. P., Staudigel, H., Pringle, M. S., & Wijbrans, J. R. (2003). Short-lived and discontinuous intraplate volcanism in the South Pacific: Hot spots or extensional volcanism? *Geochemistry, Geophysics, Geosystems*, *4*(10), 1089. https://doi.org/10.1029/2003GC000533

Koppers, A. A. P., Staudigel, H., Wijbrans, H. J. R., & Pringle, M. S. (1998). The Magellan seamount trail: Implications for Cretaceous hotspot volcanism and absolute Pacific plate motion. *Earth and Planetary Science Letters*, *163*(1–4), 53–68. https://doi.org/10.1016/s0012-821x(98)00175-7

Lee, T.-G., Lee, S.-M., Moon, J.-W., & Lee, K. (2003). Paleomagnetic investigation of seamounts in the vicinity of Ogasawara Fracture Zone northwest of the Marshall Island, western Pacific. *Earth Planets and Space*, *55*(6), 355–360. https://doi.org/10.1186/bf03351769

Lourenco, J. S., & Morrison, H. F. (1973). Vector magnetic anomalies derived from measurements of a single component of the field. *Geophysics*, *38*(2), 359–368. https://doi.org/10.1190/1.1440346

Maia, M., Dyment, J., & Jouannetaud, D. (2005). Constraints on age and construction process of the Foundation chain submarine volcanoes from magnetic modelling. *Earth and Planetary Science Letters*, *235*(1–2), 183–199. https://doi.org/10.1016/j.epsl.2005.02.044

Maus, S., Barckhausen, U., Berkenbosch, H., Bournas, N., Brozena, J., Childers, V., et al. (2009). EMAG2: A 2-arc-min resolution Earth Magnetic Anomaly Grid compiled from satellite, airborne and marine magnetic measurements. *Geochemistry, Geophysics, Geosystems*, *10*(8), Q08005. https://doi.org/10.1029/2009GC002471

McNutt, M. (1986). Nonuniform magnetization of seamounts: A least squares approach. *Journal of Geophysical Research*, *91*(B3), 3686–3700. https://doi.org/10.1029/jb091ib03p03686

NOAA National Geophysical Data Center. (1977). *Marine trackline geophysical database*. NOAA National Centers for Environmental Information. https://doi.org/10.7289/V5CZ35DR

Ogg, J. G. (2020). Geomagnetic polarity time scale. Chapter 5. In F. M. Gradstein, J. G. Ogg, M. Schmitz, & G. Ogg (Eds.), *A geological time scale 2012* (pp. 159–192). Elsevier.

Parker, R. L. (1988). A statistical theory of seamount magnetism. *Journal of Geophysical Research*, *93*(B4), 3105–3115. https://doi.org/10.1029/jb093ib04p03105

Parker, R. L., Shure, L., & Hildebrand, J. A. (1987). The application of inverse theory to seamount magnetism. *Review of Geophysics*, *25*(1), 17–40. https://doi.org/10.1029/rg025i001p00017

Phillips, J. D. (2004). Can we estimate total magnetization directions from aeromagnetic data using Helbig's integrals? *Earth Planets and Space*, *57*(8), 681–689. https://doi.org/10.1186/bf03351848

Purucker, M. E. (1990). The computation of vector magnetic anomalies: A comparison of techniques and errors. *Physics of the Earth and Planetary Interiors*, *62*(3–4), 231–245. https://doi.org/10.1016/0031-9201(90)90168-w

Romano, V., Gregg, P. M., Zhan, Y., Fornari, D. J., Perfit, M. R., Wanless, D., et al. (2022). The formation of the 8° 20′ N seamount chain, east Pacific rise. *Marine Geophysical Researches*, *43*(4), 42. https://doi.org/10.1007/s11001-022-09502-z

Ryan, W. B. F., Carbotte, S. M., Coplan, J., O'Hara, S., Melkonian, A., Arko, R., et al. (2009). Global Multi-Resolution Topography (GMRT) synthesis data set. *Geochemistry, Geophysics, Geosystems*, *10*(3), Q03014. https://doi.org/10.1029/2008GC002332

Sager, W. W. (2007). Divergence between paleomagnetic and hotspot-model-predicted polar wander for the Pacific plate with implications for hotspot fixity. *Geological Society of America Special Paper*, *430*, 335–357.

Sager, W. W., & Koppers, A. A. P. (2000). Late Cretaceous Polar Wander of the Pacific Plate: Evidence of a rapid True Polar Wander event. *Science*, *287*(5452), 455–459. https://doi.org/10.1126/science.287.5452.455

Sager, W. W., Lamarche, A. J., & Kopp, C. (2005). Paleomagnetic modeling of seamounts near the Hawaiian-Emperor bend. *Tectonophysics*, *405*(1–4), 121–140. https://doi.org/10.1016/j.tecto.2005.05.018

Scheirer, D. S., Forsyth, D. W., Cormier, M.-H., & MacDonald, K. C. (1998). Shipboard geophysical indications of asymmetry and melt production beneath the East Pacific Rise near the MELT experiment. *Science*, *280*(5367), 1221–1224. https://doi.org/10.1126/science.280.5367.1221

Scheirer, D. S., MacDonald, K. C., Forsyth, D. W., & Shen, Y. (1995). Abundant Seamount of the Rano Rahi Seamount Field near the Southern Easp Pacific Rise, 15°S to 19°S. *Marine Geophysical Researches*, *18*(1), 13–52. https://doi.org/10.1007/bf00286202

Shen, Y., Forsyth, D. W., Scheirer, D. S., & MacDonald, K. C. (1993). Two forms of volcanism: Implications for mantle flow and off-axis crustal production on the West flank of the Southern East Pacific Rise. *Journal of Geophysical Research*, *98*(B10), 17875–17889. https://doi.org/10.1029/93jb01721

Sinton, J., Bergmanis, E., Rubin, K., Batisza, R., Gregg, T. K. P., Grönvold, K., et al. (2002). Volcanic eruptions on mid-ocean ridges: New evidence from the superfast spreading East Pacific Rise, 17°–19°S. *Journal of Geophysical Research*, *107*(B6), 2115. https://doi.org/10.1029/2000JB000090

Sinton, J. M., Smaglik, S. M., Mahoney, J. J., & MacDonald, K. C. (1991). Magmatic processes at superfast spreading mid-ocean ridges: Glass compositional variations along the East Pacific Rise 13°–23°S. *Journal of Geophysical Research*, *96*(B4), 6133–6155. https://doi.org/10.1029/90jb02454

Smith, W. H. F., Staudigel, H., Watts, A. B., & Pringle, M. S. (1989). The Magellan seamounts: Early Cretaceous record of the south Pacific isotopic and thermal anomaly. *Journal of Geophysical Research*, *94*(B8), 10501–10523. https://doi.org/10.1029/jb094ib08p10501

Turcotte, D. L. (1997). *Fractals and chaos in geology and geophysics* (2nd ed.). Cambridge University Press.

White, S. M., MacDonald, K. C., Scheirer, D. S., & Cormier, M.-H. (1998). Distribution of isolated volcanoes on the flanks of the East Pacific Rise, 15.3°S–20°S. *Journal of Geophysical Research*, *103*(B12), 30371–30384. https://doi.org/10.1029/98jb02791

Zheng, L., Gordon, R. G., & Woodworth, D. (2018). Pacific plate apparent polar wander, hot spot fixity, and true polar wander during the formation of the Hawaiian Island and seamount chain from an analysis of the skewness of magnetic anomaly 20r (44 Ma). *Tectonics*, *37*(7), 2094–2105. https://doi.org/10.1029/2017TC004897